Available online at www.sciencedirect.com
SCIENCE DIRECT®
Signal Processing 86 (2006) 2744–2759
SIGNAL PROCESSING
www.elsevier.com/locate/sigpro

Recognition of the "fractional" kinetics in complex systems: Dielectric properties of fresh fruits and vegetables from 0.01 to 1.8 GHz

R.R. Nigmatullin[a,*], S.O. Nelson[b]

[a]Theoretical Physics Department, Physical Faculty, Kazan State University, 420008 Kazan, Tatarstan, Russian Federation
[b]US Department of Agriculture, Agricultural Research Service, Richard B. Russell Agricultural Research Center, P.O. Box 5677, Athens, GA 30604-5677, USA

Received 12 April 2005; received in revised form 29 October 2005; accepted 6 December 2005
Available online 10 March 2006

Abstract

Based on the new theoretical approach and the self-consistent iteration procedure for calculating the limiting values ($\varepsilon(\infty)$ and $\varepsilon(0)$) of the frequency-dependent permittivity, it becomes possible to recognize the fitting function for the function $\varepsilon(j\omega)$ measured for a complex system representing plant tissues of fresh fruits and vegetables in the frequency range (10^7–1.8×10^9 Hz). The recognized fitting function is common for all of a set of nine fruits and vegetables (apple, avocado, banana, cantaloupe, carrot, cucumber, grape, orange, and potato) and contains seven fitting parameters. These parameters are varied for different fruits and vegetables, and their behavior with respect to temperature is different but nevertheless exhibits some common features. This fitting function containing power-law exponents and confirming the existence of relaxation processes described in terms of fractional kinetic equations for some complex biological systems can be used for practical purposes to construct a desired calibration curve with respect to quality factors, as for example, moisture content or degree of maturity. The discovered common "universality" in dielectric behavior of such complex materials as plant tissues opens a possibility to use dielectric spectroscopy as a nondestructive method of control in analysis of electrical behavior (measured in the form of complex permittivity or impedance) for other complex materials.

Keywords: Theory of dielectric relaxation in plant tissues; Averaged collective motion in mesoscale region; General decoupling procedure in the Mori–Zwanzig formalism; Dielectric permittivity of fresh fruits and vegetables; Explanation of Jonscher's "universal" response

1. Introduction

Dielectric spectroscopy (DS), as a non-resonant method for investigating electrical properties of different substances, is widely used for practical applications including measurements on biological tissues and various materials of non-crystalline nature. But before one can increase the limits of applicability of this rather simple and effective method for investigating the structure of different materials, it is necessary to understand *how* the measured fitting parameters are related to the structure of the material considered. In fact, it is necessary to find a proper answer for a simple question: *what kind of information related to the structure of a material and its dynamic properties can*

*Corresponding author. Tel.: +7 8432 36061; fax: +7 8432 724093.
E-mail address: nigmat@knet.ru (R.R. Nigmatullin).

0165-1684/$ - see front matter © 2006 Elsevier B.V. All rights reserved.
doi:10.1016/j.sigpro.2006.02.018

be 'extracted' with the help of the measured complex susceptibility or impedance?

Unfortunately, the possibilities of the existing theory of relaxation cannot serve the needs of broadband DS using modern and efficient experimental techniques. Empirical relationships like the Havriliak–Negami (HN) expressions (see details in the next section) are widely used for the fitting of the complex permittivity expression. However, when the fitting parameters are not related to the structure of the material, this is the main obstacle for increasing of the limits of applicability of DS. The main purpose of this paper is to find the proper answer for the question formulated above. Besides, we want to demonstrate these new possibilities in analysis of such complex materials as plant tissues of different fresh fruits and vegetables. The reduction of a different set of micromotions to the averaged collective motion in the mesoscale region helps in understanding true possibilities of DS among other 'spectroscopies'. We can define DS as the spectroscopy of *different collective motions*. In other words, the process of treating dielectric relaxation in self-similar structures in the mesoscale region is *simplified*. We have only a few collective motions appearing in the results of the averaging procedure, described in detail in the next section, that interact with each other. This important mathematical result helps to increase the possibilities of DS and applies to a wide class of non-crystalline materials of different complexity, including, for example, different biological cells and tissues. In this paper, we chose plant tissues of different fruits and vegetables to demonstrate the fact that the identified complex permittivity function looks rather simple and reflects the contribution of different collective motions interacting with each other in the intermediate range of scales.

Having in mind the practical side of DS, we can note that the dielectric properties of different complex materials can be used to sense non-electrical characteristics of those materials when the permittivities, or dielectric properties, of those materials are correlated with the non-electrical material characteristics. An excellent example is found in the agricultural industry [1], where, for example, the moisture content of cereal grains and other seed crops must be determined rapidly at harvest and times of sale. The moisture content, or proportion of water in these materials, is critical for safe storage, because the materials will be infected with fungi and spoil if the moisture content is too great. Standard methods of moisture content determination require oven drying for time periods ranging from 1 to 36 h at specified temperatures, so electronic moisture meters that sense moisture immediately through the correlation between permittivity and moisture content have been developed and used in commerce for many years [1,2].

Complex relative permittivities of fresh fruits and vegetables have been measured at microwave frequencies to determine whether these properties might be useful in determining maturity of peaches, *Prunus persica* (L.) Batsch or chilling injury in sweet potatoes, *Ipomoea batatas* (L.) Lam. [3,4]. Results indicated that such measurements at a single frequency cannot be expected to be useful in distinguishing stage of maturity or injury. With the availability of test equipment and techniques for wide frequency-range permittivity measurements, additional permittivity measurements on fresh fruits and vegetables were obtained between 0.2 and 20 GHz [5], and efforts were also made to distinguish differences in maturity of peaches [6]. Differences in the real part of the permittivity due to maturity stage were noted at the lower end of the frequency range, and lesser differences in the imaginary part were noted at the higher frequencies. Differences in the real part of the permittivity appeared to be diverging at the lower frequencies, so interest was indicated in such measurements at lower frequencies.

Therefore DS data were obtained over the frequency range from 10 MHz to 1.8 GHz for several fresh fruits and vegetables, providing permittivities as a function of both frequency and temperature [7]. These data have provided an opportunity for further study by advanced dielectric relaxation analysis, which is also the main subject of this paper.

2. Reduction of a set of micromotions to the averaged collective motion on mesoscale

In DS, there is one contradictory point that should be understood in detail. On one hand, dielectric/impedance spectroscopy is applicable for a wide class of substances having different geometric configurations, different physical structures and types of systems (crystals, polymers, films, biological tissues, etc.), and a variety of polarizing species (dipoles, hopping electrons, polarons, ions) with respect to the applied electric field. On the other hand, in spite of such a variety of substances, the measured complex permittivity is described

by a few fitting functions (in most cases having empirical origin) containing presumably a set of power-law exponents. The most popular function used for the fitting of complex permittivity is the HN equation [8]

$$\varepsilon^*_{\mathrm{HN}}(\mathrm{j}\omega) = \varepsilon'(\omega) - \mathrm{j}\varepsilon''(\omega) = \varepsilon_\infty + \frac{\varepsilon_\mathrm{s} - \varepsilon_\infty}{(1 + (\mathrm{j}\omega)^\nu)^\beta}. \quad (1)$$

Here, $\varepsilon^*_{\mathrm{HN}}(\mathrm{j}\omega)$ is the HN complex permittivity with real and imaginary components $\varepsilon'(\omega)$ and $\varepsilon''(\omega)$, respectively. Here $\varepsilon_\mathrm{s} = \varepsilon'(0)$ is the static complex permittivity, ε_∞ is a value of permittivity at higher (phonon) frequencies (10^{12}–10^{13} Hz), ν and β are some *empirical* power-law exponents not having clear physical meaning. Traditionally, the measured permittivity-frequency data are interpreted and analyzed quantitatively using expression (1) or its linear combinations. However, in this description the fitting parameters ν and β remain empirical, and the desired relationship with structural or microscopic motion parameters of the material considered is *not* known. Other approaches describing non-Debye relaxation in complex materials are given in a recent review [9].

The fact that different dielectric spectra are described by the functions containing a combination of the power-law exponents is confirmed in dielectric measurements realized by Jonscher with co-authors [10] for a wide class of various substances. He formulated the so-called "universal" response (UR) phenomenon when the branches of dielectric spectra (expressed in the form of complex susceptibility) are described by expressions

$$\chi(\mathrm{j}\omega) = C_n(\mathrm{j}\omega)^{-1+n},$$
$$\chi(\mathrm{j}\omega) = A_m - B_m(\mathrm{j}\omega)^m, \quad 0 < m, n < 1. \quad (2)$$

Finally, expressions (2) serve as the *definition* of the UR behavior. Here m and n are some real power-law exponents usually located in the interval [0,1]. The validity of expressions (2) are realized always in some finite frequency range $\omega_{\min} < \omega < \omega_{\mathrm{Mx}}$.

So, the natural question is realized: how to understand the UR phenomenon expressed in the form (2) observed in a wide class of dielectric materials? In other words, what do we really measure in different materials by means of complex permittivity data?

In this section, we want to show *how* a set of different micromotions in the mesoscale region is averaged and transformed to some collective motion that is expressed analytically in the form of the UR response behavior. This rigorous mathematical result gives a natural explanation for the UR phenomenon and explains the fact that DS is the spectroscopy of collective motions.

Our starting point is based on the Mori–Zwanzig theory [11] that is widely used for description of kinetic properties of many complex systems [12–15]. In DS, this approach was applied recently to the description of the properties of water molecules [16]. The chain of equations for an arbitrary time correlation function (in our case proportional to the total polarization $P(t)$) can be written as [16,17]

$$\frac{\mathrm{d}P(t)}{\mathrm{d}t} = -\int_{t_0}^{t} k_1(t-u)P(u)\,\mathrm{d}u,$$
$$\frac{\mathrm{d}k_1(t)}{\mathrm{d}t} = -\int_{t_0}^{t} k_2(t-u)k_1(u)\,\mathrm{d}u, \quad (3)$$

where $k_1(t)$, $k_2(t)$ are the memory functions of the corresponding orders including the equilibrium frequency moments. The basic problem in using the Mori–Zwanzig formalism is to make a reasonable decoupling *assumption* for the memory function in order to truncate the infinite chain of integro-differential equations.

Having in mind the confirmation of the phenomenological approach developed earlier [18–20] from basic statistical principles, we present the first equation in the form

$$P(t) - P(t_0) + \int_{t_0}^{t} M(t-u)P(u)\,\mathrm{d}u = 0,$$
$$M(t) = \int_{t_0}^{t} (t-u)k_1(u)\,\mathrm{d}u. \quad (4)$$

The reason for such presentation is that the Mori–Zwanzig equations cannot describe *broadened* dielectric spectra. Previous attempts to describe the broadened spectra from the Mori–Zwanzig equations presented in form (3) for different memory functions were unsuccessful [21]. Probably, it is related to the fact that in nature there is a wide class of processes that are changed more slowly in comparison with the velocity of a relaxation process, which is usually associated with the first derivative. Such relaxation process is described by a kinetic equation with derivative less than the first order

$$D^\nu_0 \tau^\nu P(t) + P(t) = 0. \quad (5)$$

Here D^ν_0 determines the Riemann–Liouville fractional operator [22]. Eq. (5) leads in the frequency domain to the well-known Cole–Cole expression for the complex susceptibility [22,23]. Such type of kinetic equations cannot be derived directly from the

conventional Mori–Zwanzig formalism [12–15], and new investigations in receiving the 'pure' integral equations for description of slow relaxation processes are *necessary*.

In this paper, we suggest a rather general decoupling procedure related to the approximate calculation of the memory function $M(t)$. For further purposes it is convenient to consider the memory function $M(t)$ as a function of the Laplace parameter s. Putting $t_0 = 0$ and applying the Laplace transform to Eq. (4) we obtain

$$P(s) + M(s)P(s) = \frac{P(0)}{s}. \tag{6}$$

To find an analytical expression for the Laplace-image of the memory function $M(s)$ describing a relaxation/exchange process with thermostat, we suppose that:

A1. We consider a heterogeneous material having a self-similar structure. This structure can be presented by a set of electrically active clusters. Each cluster includes a group of strongly correlated dipoles. However, different clusters are weakly correlated with each other.

A2. The relaxation/exchange process with a thermostat in some volume V_n is described by a microscopic function $f(s\tau_n)$. Here τ_n is a characteristic relaxation time describing the relaxation/exchange process with the thermostat for a group of strongly correlated dipoles located in a cluster having the volume V_n. If the nth cluster contains N_n number of dipoles then the relaxation/exchange process with the thermostat of a set of weakly correlated clusters is described by the function:

$$M(s) = \sum_n N_n f(s\tau_n). \tag{7}$$

This expression increases the limits (when $N_n \neq 1$) of applicability of the additivity hypothesis widely used in statistical mechanics for a set of weakly correlated physical values.

A3. Without loss of generality, we may suppose that the Laplace-image of the function $f(z)$ depending on the complex variable z and describing the microscopic act of interaction of an electric dipole with the thermostat has the following form:

$$f(z) = \frac{a_0 + a_1 z + \cdots + a_K z^K}{b_0 + b_1 z + \cdots + b_P z^P} \tag{8}$$

with $K \leqslant P+1$, and the polynomial in the denominator has an only negative and complex-conjugate root.

Case (a): $\mathrm{Re}(z) \ll 1$ $(c_0 = a_0/b_0, \quad c_1 = a_1/b_0 - b_1/b_0^2)$

$$f(z) = c_0 - c_1 z + c_2 z^2 + \cdots. \tag{9a}$$

Case (b) $\mathrm{Re}(z) \gg 1$ $(A_1 = a_K/b_P, \quad A_2 = a_K b_{P-1}/b_P^2)$

$$f(z) = \frac{A_1}{z^{P-K}} + \frac{A_2}{z^{P-K+1}} + \cdots. \tag{9b}$$

For $K = P+1$ we define $f(z)$ as a *relaxation* function describing the process of interaction of a dipole with a thermostat. If $K < P+1$ and the denominator of polynomial (9) has divisible roots, then we define $f(z)$ as an *exchange* function describing the interaction process of a dipole with thermostat. The reason for such division is that the minimal value of the function $f(t) \overset{\mathrm{LT}}{=} f(s)$ in the first case is $f(0) \neq 0$, and moreover $f(t)$ goes to zero as $t \to \infty$ *monotonically*. In the exchange case, however, the value $f(0) = 0$ and the microscopic function $f(t)$ has at least one maximum and so may tend to zero monotonically or nonmonotonically as $t \to \infty$.

A4. We assume that the distributions of the values N_n and the set of relaxation times τ_n obey the following scaling conditions:

$$N_n = N_0 b^n,$$
$$\tau_n = \tau_0 \xi^n \quad (-N < n < N, \quad N \gg 1, \quad b, \quad \xi > 0). \tag{10}$$

At $n = 0$ we define the number of dipoles N_0 and the characteristic relaxation time τ_0, respectively, for the cluster having a minimum number of correlated dipoles. Without loss of generality, one can assume that the volume of the minimum cluster coincides with one dipole. So, $N_0 = 1$ and τ_0 defines the characteristic time of the relaxation/exchange process with thermostat of a single dipole.

The above suppositions mean that the expression for the Laplace-image of the memory function $M(t)$ assumes the form

$$M(z) \equiv S(z) = \sum_{n=-(N-1)}^{N-1} b^n f(z\xi^n), \quad (N \gg 1). \tag{11}$$

Here $z \equiv s\tau_0$. Moreover, the function $S(z)$ at any fixed N satisfies the functional equation

$$S(z\xi) = \frac{1}{b}S(z) + b^{N-1}f(z\xi^N) - b^{-N}f(z\xi^{-N+1}). \quad (12)$$

We consider the asymptotic solution of this scaling equation at $N \gg 1$ for b and $\xi < 1$.

Taking into account the asymptotic behavior of the function $f(z)$ at small (9a) and large (9b) values of Re(z), the contribution of the last two terms in (12) becomes negligible for the interval:

$$z_{\min} | z | z_{\max}. \quad (13)$$

Here

$$z_{\min} = \left(\frac{A_1}{b^N}\right)^{1/(P-K)} \xi^{N-1}, \quad z_{\max} = \frac{b}{(b\xi)^N}. \quad (14)$$

For interval (13) at $N \gg 1$, the scaling Eq. (13) is simplified and takes the form

$$S(z\xi) = \frac{1}{b}S(z). \quad (15)$$

The general solution of this scaling equation can be written as [23]

$$S(z) = \pi_v(\ln z)z^{-v}, \quad v = \frac{\ln(1/b)}{\ln(1/\xi)}. \quad (16)$$

Here $\pi_v(\ln z \pm \ln \xi) = \pi_v(\ln z)$ is a complex log-period function with real period $\ln(\xi)$. The geometrical/physical meaning of this function and methods for its calculation have been considered previously [24]. If we approximately replace $S(z)$ in (12) by integration, then one can evaluate the zeroth Fourier component of the function $\pi v(\ln z)$. We define this component using condition

$$\langle \pi_v(\ln z) \rangle z^{-v} \approx \int_{u=-N+1}^{N-1} b^u f(z\xi^u)\, \mathrm{d}u. \quad (17)$$

Taking into account the asymptotic decompositions (9) and condition b, $\xi < 1$ one can obtain the following expression from (17)

$$\langle \pi_v(\ln z) \rangle \equiv C_0(v) = \frac{1}{\ln(1/\xi)} \int_0^\infty x^{v-1} f(x)\, \mathrm{d}x. \quad (18)$$

By analogy with these calculations, one can consider other conditions imposed on parameters b and ξ. All these cases have been considered and presented in Table 1.

Analyzing these cases, one can say that relaxation/exchange processes with thermostat taking place in a system of self-similar clusters are reduced to the memory function

$$M(z) = C_0 z^{\pm v} + C_1 z^{\pm v + \mathrm{j}\langle\Omega\rangle} + C_1^* z^{\pm v - \mathrm{j}\langle\Omega\rangle} x. \quad (19)$$

Here the real power-law exponent v accepts positive or negative values and so its values are not limited to the interval $(0 \leqslant |v| \leqslant 1)$. The

Table 1
Various solutions of the asymptotic scaling Eq. (16) for particular values of the scaling parameters b and ξ

Case	Values of b	Values of ξ	$\omega_{\min}$	$\omega_{\max}$	Functional equation	Solution
1.	$b<1$	$\xi<1$	$\xi^{N-1}\left(\frac{A_1}{b^N}\right)^{1/(P-K)}$	$\frac{b}{(b\xi)^N}$	$S(z\xi) = \frac{1}{b}S(z)$	$S(z) = \pi_v(\ln z)z^{-v}$, $v = \frac{\ln(1/b)}{\ln(1/\xi)}$
2.	$b>1$	$\xi<1$	$\xi^{N-1}\left(\frac{A_1}{b^N}\right)^{1/(P-K)}$	$\frac{b}{(b\xi)^N}$	$S(z\xi) = \frac{1}{b}S(z) + r_0$, $r_0 = c_0 b^{N-1}$ is finite value	$S(z) = \pi_v(\ln z)z^v + \frac{br_0}{b-1}$, $v = \frac{\ln(b)}{\ln(1/\xi)}$
3.	$b<1$	$\xi>1$	$\frac{(A_1 b^{N-1})^{1/(P-K)}}{\xi^N}$	$\frac{(b\xi)^N}{c_1\xi}$	$S(z\xi) = \frac{1}{b}S(z) + r_0$, $r_0 = c_0 b^{N-1}$ is finite value	$S(z) = \pi_v(\ln z)z^v - \frac{br_0}{1-b}$, $v = \frac{\ln(1/b)}{\ln(\xi)}$
4.	$b>1$	$\xi>1$	$\frac{(A_1 b^{N-1})^{1/(P-K)}}{\xi^N}$	$\frac{(b\xi)^N}{c_1\xi}$	$S(z\xi) = \frac{1}{b}S(z)$	$S(z) = \pi_v(\ln z)z^{-v}$, $v = \frac{\ln(1/b)}{\ln(1/\xi)}$
5.	$b=1$	$\xi<1$	$(A_1)^{1/(P-K)}\xi^{N-1}$	$c_1\xi^{-N}$	$S(z\xi) = S(z) + c_0$	$S(z) = \pi_0(\ln z) + c_0\frac{\ln(z)}{\ln(\xi)}$

mode $\langle\Omega\rangle$ figuring in (19) is appearing because of the approximate replacement of the exact log-periodic function $\pi v[\ln(z)]$ in (16) by one mode, i.e.

$$\pi_v(\ln z) \cong C_0(v) + C_1 \exp(\mathrm{j}\langle\Omega\rangle) + C_1^* \exp(-\mathrm{j}\langle\Omega\rangle). \tag{20}$$

For the random fractals two terms figuring in (20) are becoming negligible and the memory function in (19) is reduced to the well-known constant phase-angle element (CPE) [10]

$$M(\mathrm{j}\omega) \equiv Z_v(\mathrm{j}\omega) = C_0(v)(\mathrm{j}\omega)^{\pm v}. \tag{21}$$

Here the parameter $C_0(\mathrm{v})$ is defined by expression (18). The Laplace complex parameter s is identified with the complex frequency as $s \equiv \mathrm{j}\omega$.

Suppose now that the initial memory function $M(t)$ in (4) is modified by an exponential damping function and is written as

$$M(t) = \int_0^t (t-u)k_1(u)\,\mathrm{e}^{-\lambda u}\,\mathrm{d}u. \tag{22}$$

In this case the Laplace variable is shifted by the value $z+\lambda\tau_0$. If we suppose that only one collective mode exists, then the reduction procedure described above leads to the following generalized expression for the memory function in the frequency domain:

$$M(\mathrm{j}\omega) = C_0(\lambda\tau_0 + \mathrm{j}\omega\tau_0)^{\pm v} + C_1(\lambda\tau_0 + \mathrm{j}\omega\tau_0)^{\pm v + \mathrm{j}\langle\Omega\rangle} + C_1^*(\lambda\tau_0 + \mathrm{j}\omega\tau_0)^{\pm v - \mathrm{j}\langle\Omega\rangle}. \tag{23}$$

It is natural to define this function as the *generalized* (when $\langle\Omega\rangle \neq 0$) impedance function describing the behavior of the so-called *reind* (*re*sistance + *ind*uctance, $v>0$) and *recap* (*re*sistance + *cap*acitance, $v<0$) two-pole element, respectively. Below we shall use the abbreviation, the generalized recap/reind element (GRE) for the memory function satisfying relationship (23).

So, finishing this section one can conclude that the reduction of a set of different micromotions to the averaged collective motion naturally explains and generalizes the UR phenomenon. In fact, this procedure helps in understanding the *unique* place of DS; this spectroscopy can be identified as the spectroscopy of different collective motions interacting with each other in the mesoscale region. It explains also, from the microscopic positions, the data-curve fitting approach developed previously as a phenomenological tool for the fitting of raw complex permittivity data in the frequency domain [18–20]. According to this approach the complex permittivity in the absence of the constant conductivity can be written in the form [18,20]

$$\varepsilon(\mathrm{j}\omega) = \varepsilon_\infty + \frac{\varepsilon_\mathrm{s} - \varepsilon_\infty}{1 + R(\mathrm{j}\omega)},$$
$$R(\mathrm{j}\omega) = \left[(\mathrm{j}\omega\tau_1)^{\pm v_1} + (\mathrm{j}\omega\tau_2)^{\pm v_2}\right]^{\pm 1}. \tag{24}$$

The last expression $R(\mathrm{j}\omega)$ is correct for the case of two collective motions. These motions expressed in the form of recap two-pole elements can be connected with each other in parallel ($v_{1,2}>0$) or in series ($v_{1,2}<0$). Taking into account the general expression for the memory function (23), which is correct for a wide class of self-similar structures, this expression can be easily generalized for a set of collective motions exceeding two and for the case of quasi-regular fractals when $\langle\Omega\rangle \neq 0$.

3. Materials and experimental methods

Detailed information about the sample materials and methods used for the permittivity measurements is available elsewhere [7], but pertinent information of interest will be included here.

3.1. Fruits and vegetables

A few samples of fresh fruits and vegetables were selected to study the variation of permittivity with temperature and frequency in the range from 10 MHz to 1.8 GHz. They included the 'Red Delicious' apple, *Malus domestica* Borkh.; Navel orange, *Citrus aurantium* subsp. bergamia; 'Thompson Seedless' grape, *Vitis amurensis* Rupr.; 'Cavendish' banana, *Musa x paradisiacal* L. var. paradisiacal; 'Russett Burbank' potato, *Solanum tuberosum* L.; cucumber, *Cucumis sativus* L.; carrot, *Daucus carota* subsp. sativus (Hoffm.) Arcang.; cantaloupe, *Cucumis melo* L.; and avocado, *Persea Americana*, Miller var. americana.

3.2. Permittivity measurements

The electrical measurements necessary for permittivity determination were obtained with a Hewlett-Packard[1] 85070B open-ended coaxial-line probe, a Hewlett-Packard 4291A Impedance/Material Analyzer, and a temperature-controlled stainless steel sample cup and water jacket assembly (Fig. 1), designed and built for use with the 85070B

[1]Mention of company or trade names is for purpose of description only and does not imply endorsement by the US Department of Agriculture.

probe [8]. Permittivities were calculated with Agilent Technologies 85070D Dielectric Probe Kit Software, modified for use with the HP 4291A Analyzer by Innovative Measurement Solutions, which provided permittivity values from the reflection coefficient of the material in contact with the active tip of the probe [9].

Sample temperature control was provided by circulating water through the jacket surrounding the sample cup from a Haake B3 Constant Temperature Circulator with a digital control module. Sample cup temperature was monitored with a No. 36 B & S gage duplex nylon-insulated copper–constantan thermocouple and a Digi-Sense JTEK Thermocouple Thermometer. The thermocouple was inserted into the 0.9-mm hole in the 1.64-mm thick sidewall of the sample cup.

3.3. Sample preparation and physical measurements

Samples to fit snugly in the 18.95-mm diameter sample cup for efficient heat transfer were obtained from a slice of the fruit or vegetable with stainless steel cork-borer-type sample cutters fabricated for the purpose.

Tissue sample densities were obtained by weighing the sample on an analytical balance, measuring the diameter and length of the sample with a dial caliper, calculating the volume, and then dividing the sample weight by this volume to obtain the density. Moisture contents of fruit and vegetable tissue samples were obtained by drying them in disposable aluminum weighing dishes for 16 h at 100 °C in a forced-air oven. Upon removal from the oven, the weighing dishes and samples were cooled in a desiccator equipped with anhydrous calcium sulfate (Drierite) before reweighing to determine sample moisture loss. Moisture contents were calculated for reporting on a wet weight basis.

Percentage of total soluble solids, mainly sugars in fruits, was determined by expressing juice from samples and taking measurements with a Bausch and Lomb Abbe 3L refractometer. Samples for moisture and refractometer tests were generally taken from the same slice as the sample for permittivity measurement or from adjacent tissue. For grapes, which were only large enough for the sample required for permittivity measurements, moisture and refractometer tests were run on the ends cut from the grape to provide two parallel surfaces and on additional grapes from the same bunch.

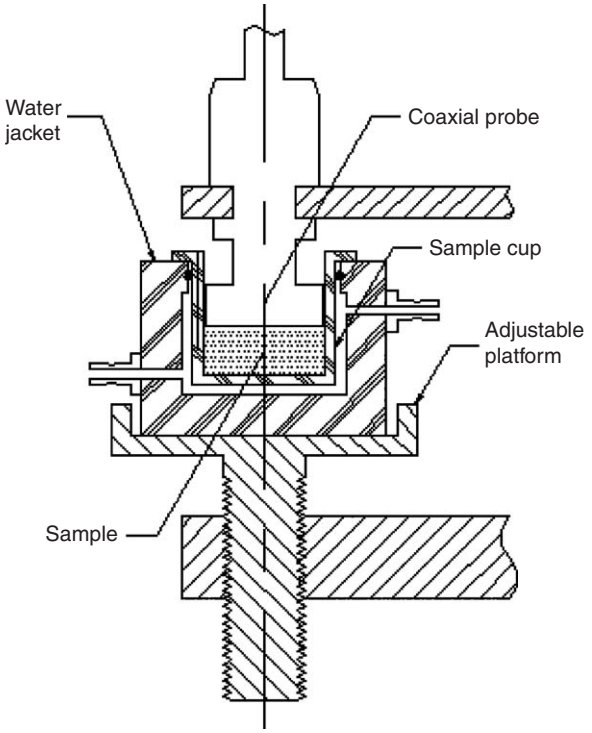

Fig. 1. Sectional view of stainless steel sample cup for open-ended coaxial-line probe permittivity measurements: Delrin water jacket for temperature control, and supporting platform for water jacket and sample cup assembly, showing portions of supporting clamps for probe and water jacket platform.

3.4. Measurement procedures

The HP 4291A Analyzer was permitted to warm up for at least 1 h for stabilization. The computer program was then initiated which performed the instrument setup. The analyzer was calibrated by connecting an open- and short-circuit termination and a matched load in sequence to the 7-mm precision connector of the HP 4291A High Impedance Test Head used with the analyzer. Next, the cable for the HP 85070A Dielectric Probe was connected to the Test Head and given several minutes to stabilize from slight flexure. The probe was already clamped in position on the probe stand and the cable had already been supported in nearly the same position to avoid any temporal disturbances due to changes in cable position or flexure. Then, the probe calibration was completed by using the air, short-circuit, and glass-distilled water references, and measurements were made on air and distilled water to verify that proper permittivity values were being obtained. The 25 °C distilled water reference was raised to the probe in a 10-ml

glass beaker so that visual inspection could insure there were no air bubbles trapped in the measurement region at the tip of the probe.

Generally, slices about 1.5 cm thick were cut from the fruit or vegetable with a sharp knife, cutting the surfaces as nearly parallel as possible. These cuts were made in planes perpendicular to the axis of symmetry or longitudinal axis of the fruit or vegetable, taking the slice from the central region. The slice was then immediately transferred to a drill press for cutting the cylindrical sample. The sample was removed from the cutter and weighed on an analytical balance. Its dimensions were then measured with a dial caliper, and it was inserted into the sample cup in preparation for the permittivity measurements. For firm tightly fitting samples, a small vertical groove was cut in the edge of the sample to permit the escape of air as the sample was inserted into the sample cup. Then the sample cup and water jacket assembly (Fig. 1) was raised in position on the probe stand to bring the probe flange into the sample cup and the sample into contact with the tip of the probe. A permittivity measurement was triggered to insure that there was good contact between the probe and the sample.

After a few minutes to give the sample time to come into temperature equilibrium with the circulating water at 5 °C, the first permittivity measurement to be recorded was triggered, and the setting for the constant temperature circulator was raised to 15 °C. The water temperature in the circulator had been lowered to 5 °C by the addition of crushed ice. After the initial measurement for record at 5 °C, permittivity measurements were taken at 10 °C intervals up to 95 °C. The circulator made this 10 °C adjustment in the water temperature in about 2 min, and a subsequent period of 3 min was provided for the sample to equilibrate to the new temperature. Repeated permittivity measurements with no change in resulting values verified that the 3-min interval was sufficient for the temperature equilibration of the sample for the permittivity measurements. Thus, permittivity measurements and set-point adjustments were triggered at 5-min intervals, and the entire measurement sequence was completed in about 50 min. At the termination of each measurement sequence, crushed ice was introduced into the controlled temperature circulator to lower the sample temperature, and the sample was removed from the sample cup and sealed in a small jar for subsequent oven moisture tests along with samples from the fresh fruit or vegetable. Permittivity measurements on air and water were then taken to verify the stability of the probe calibration during the measurement sequence.

4. Results of measurements

The non-electrical characteristics of the fresh fruit and vegetable samples are presented in Table 2 for descriptive purposes. There are differences among the various fruits and vegetables in the characteristics shown. Cucumber tissue has the highest moisture content among those listed, and banana tissue has the lowest moisture content. Differences are also shown for tissue density, with potato having the highest density and apple having the lowest. For total soluble solids, which are mostly sugars in fruits, banana is the highest and cucumber is the lowest. All of these characteristics influence

Table 2
Characteristics of fruit and vegetable tissue samples

Fruit or vegetable	Cultivar or other description	Moisture content (%)	Tissue density (g/cm^3)	Total soluble solids (%)
Apple, *Malus domestica* Borkh.	'Red Delicious'	85	0.81	13.4
Avocado, *Persea americana* Miller var. Americana		82	0.99	8.1
Banana, *Musa x paradisiacal* L. var. Paradisiaca	'Cavendish'	74	0.98	22.3
Cantaloupe, *Cucumis melo* L.	Muskmelon	87	0.97	13.0
Carrot, *Daucus carota* subsp. sativus (Hoffm.) Arcang.		87	1.00	8.6
Cucumber, *Cucumis sativus* L.		97	0.94	2.4
Grape, *Vitis amurensis* Rupr.	'Thompson Seedless'	83	1.01	17.3
Orange, *Citrus aurantium* subsp. Bergamia	Navel	89	1.04	13.1
Potato, *Solanum tuberosum* L.	'Russett Burbank'	77	1.08	6.4

the dielectric properties, with moisture content and density expected to have the more important roles.

The variation of the dielectric properties of samples from two of these nine fruits and vegetables with frequency and temperature is shown, for example, for apple and avocado in Figs. 2 and 3. Both the real and imaginary parts of the complex relative permittivity, dielectric constant and loss factor, show monotonic decreases in value as frequency increases. Trends with temperature are not so consistent. For example, at the lowest frequency, the dielectric constant and the loss factor both increased monotonically with temperature for avocado (Fig. 3), cantaloupe, cucumber, and orange. For the other five, apple (Fig. 2), banana, carrot, grape, and potato, the dielectric constant increased as the temperature increased from 5 to 65 or 75 °C and then decreased as temperature continued to increase.

The very high values for ε' at the lower end of the frequency range are no doubt attributable to the

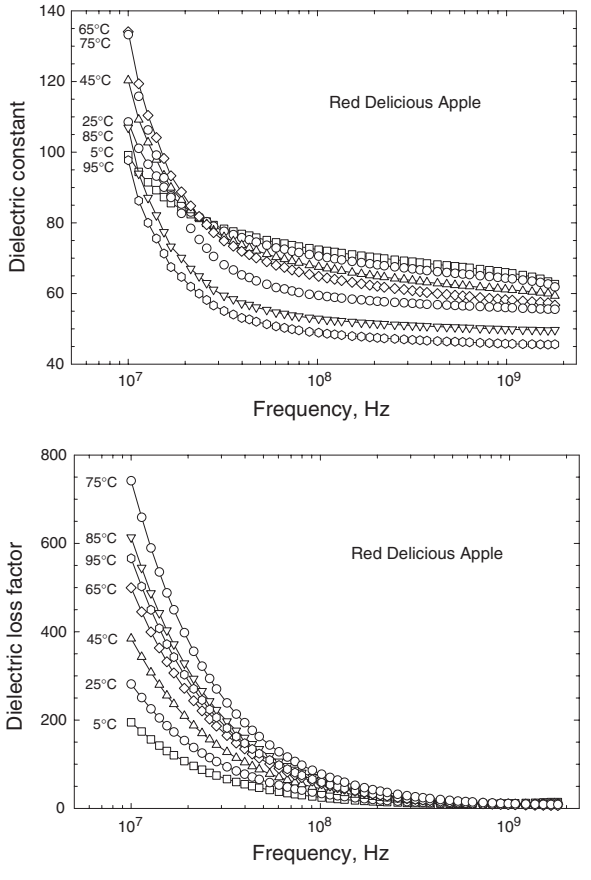

Fig. 2. Frequency and temperature dependence of apple permittivity.

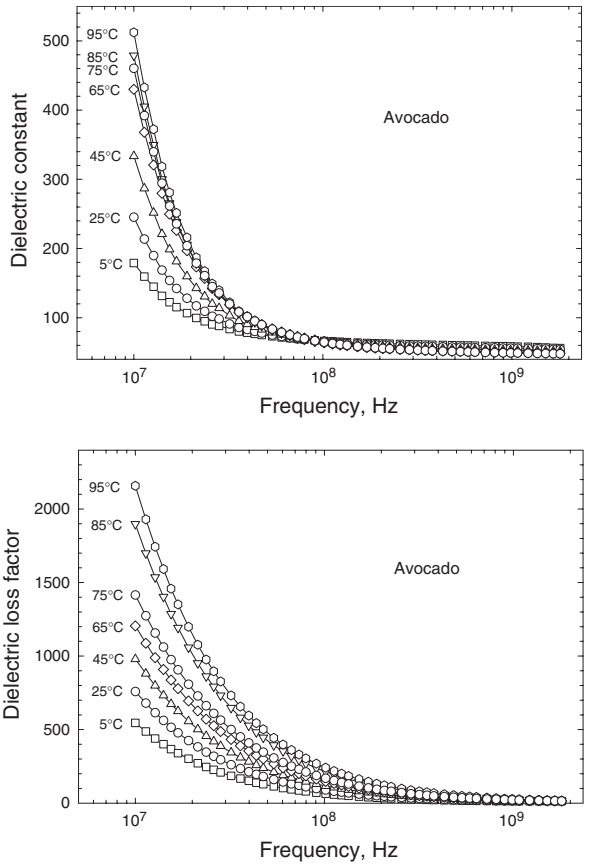

Fig. 3. Frequency and temperature dependence of avocado permittivity.

contribution of ionic conduction, while the behavior of ε' at the higher end of the frequency range is characteristic of dipolar relaxation. It is obvious in Fig. 3 that, at some frequency in the range between 10 and 100 MHz, the temperature dependence of ε' disappears, and the ionic conduction becomes the dominant mechanism influencing the value of ε' below that frequency. This is particularly clear in Fig. 3 for avocado and was also true for banana, cantaloupe, carrot, cucumber, and orange. It is less clear for apple tissue in Fig. 2 and for grape and potato, where the reversal of the temperature coefficient sign takes place in the 65–75 °C range. This change in the sign of the temperature coefficient of ε' for apple, grape, potato, and banana is probably associated with changes caused by the breakdown of cell membranes as a result of exposure to the high temperatures even for relatively short time periods. For those tissues in which the reversal of the temperature coefficient for the dielectric constant did not occur, there was a

reduction in the temperature coefficient at temperatures above about 65 °C, which can most likely be explained by the same phenomenon.

5. A general description of the recognition procedure

Expression (24) can serve as a general formula for the fitting of the measured complex permittivity data in the frequency domain. Let us suppose that another expression can be presented in the form of linear combinations of two complex functions, i.e.

$$\varepsilon(\mathrm{j}\omega) = \varepsilon_\infty + \frac{\Delta_1}{1 + R_1(\mathrm{j}\omega)} + \frac{\Delta_2}{1 + R_2(\mathrm{j}\omega)}. \tag{25}$$

Simple algebraic manipulations show that the last expression can be presented again in the form (24)

$$\varepsilon(\mathrm{j}\omega) = \varepsilon_\infty + \frac{\Delta_1 + \Delta_2}{1 + R_{12}(\mathrm{j}\omega)}, \tag{26}$$

where

$$R_{12}(\mathrm{j}\omega) = \frac{w_1 R_1(\mathrm{j}\omega) + w_2 R_2(\mathrm{j}\omega) + R_1(\mathrm{j}\omega)R_2(\mathrm{j}\omega)}{1 + w_1 R_2(\mathrm{j}\omega) + w_2 R_1(\mathrm{j}\omega)},$$
$$w_k = \frac{\Delta_k}{\Delta_1 + \Delta_2}, \quad (k = 1, 2). \tag{27}$$

The basic problem in the concrete application of expression (24) is to develop some recognition procedure which allows one to differentiate the true form of the function $R(\mathrm{j}\omega)$ and the number of power-law exponents in it. At present, a general solution of this problem is absent. Solutions of some partial problems are shown in [18]. Here we note two points that are important for treatment of raw DS data.

5.1. The recognition of the low-frequency (LF) branch

It is known that, at low frequencies in some materials displaying hopping/ionic conductivity [10], a low-frequency dispersion (LFD) phenomenon takes place. It can be detected as an increasing branch of real and complex parts of the permittivity in the LF region. In accordance with the classification given by Jonscher [10], the LFD is expressed in the form

$$\varepsilon(\mathrm{j}\omega) = \varepsilon_\infty + \frac{1}{(\mathrm{j}\omega\tau)^\theta}. \tag{28}$$

So, if the LFD phenomenon exists in some conducting material with hopping conductivity it can be detected by application of the ratio presentation (RP) format [18]. Expression (28) in RP format accepts the form

$$-\left(\frac{\mathrm{Re}[\varepsilon(\mathrm{j}\omega)]}{\mathrm{Im}[\varepsilon(\mathrm{j}\omega)]}\right) = A + B\omega^\theta,$$
$$A = \cot\left(\frac{\pi\theta}{2}\right), \quad B = \frac{\varepsilon_\infty \tau^\theta}{\sin(\pi\theta/2)}. \tag{29}$$

This behavior can be easily differentiated from the complex permittivity representing the Cole–Cole function for $R = (\mathrm{j}\omega\tau)^\nu$. In the RP format the Cole–Cole function accepts the form

$$-\left(\frac{\mathrm{Re}[\varepsilon(\mathrm{j}\omega)]}{\mathrm{Im}[\varepsilon(\mathrm{j}\omega)]}\right) = A + B\omega^{-\nu} + C\omega^\nu,$$
$$A = \left(\frac{\varepsilon_s + \varepsilon_\infty}{\varepsilon_s - \varepsilon_\infty}\right)\cot\left(\frac{\pi\nu}{2}\right),$$
$$B = \frac{\varepsilon_s}{(\varepsilon_s - \varepsilon_\infty)\tau^\nu \sin(\pi\nu/2)},$$
$$C = \frac{\varepsilon_\infty \tau^\nu}{(\varepsilon_s - \varepsilon_\infty)\sin(\pi\nu/2)}. \tag{30}$$

The last function has a specific minimum shifted presumably to the high-frequency (HF) region ($\varepsilon_s/\varepsilon_\infty > 1$) with respect to the maximum of the Cole–Cole function

$$\omega_{\min} = \left(\frac{\varepsilon_s}{\varepsilon_\infty}\right)^{1/2\nu}\frac{1}{\tau} \equiv \left(\frac{\varepsilon_s}{\varepsilon_\infty}\right)^{1/2\nu}\omega_{CC}. \tag{31}$$

Here ω_{CC} determines the maximum value of the Cole–Cole function. It helps to differentiate the LFD behavior from the Cole–Cole function. The specific features evoked by linear combination of the LFD and Cole–Cole functions are shown in [18]. So, the RP format is very informative in recognition of a possible LFD phenomenon in measured DS data.

5.2. The self-consistent calculation of the limiting values ε_s and ε_∞

Let us come back again to expression (24). For further purposes, it is convenient to present this expression in the form

$$\varepsilon(\mathrm{j}\omega; \varepsilon_\infty, \varepsilon_s) = \varepsilon_\infty + \frac{\varepsilon_s - \varepsilon_\infty}{1 + R(\mathrm{j}\omega)}. \tag{32}$$

To find the initial values, one can use the presentation of the complex permittivity in normal and modulus ($1/\varepsilon(\mathrm{j}\omega)$) formats, respectively. Here we want to note one advantage of the presentation of DS data in the modulus format that is very informative in recognition of different dielectric

spectra. Based on expression (24), after simple algebraic manipulations one can obtain the following expression:

$$\frac{1}{\varepsilon(\mathrm{j}\omega)}=\frac{1}{\varepsilon_\infty}+\left[\frac{1}{\varepsilon_\mathrm{s}}-\frac{1}{\varepsilon_\infty}\right]\frac{1}{1+\lambda R(\mathrm{j}\omega)},\quad \lambda=\frac{\varepsilon_\infty}{\varepsilon_\mathrm{s}}. \tag{33}$$

Since, $\lambda<1$ and $R(\mathrm{j}\omega)$ represents a linear combination of the power-law functions, the dielectric spectrum analyzed is artificially *shifted* from the LF to the HF region. So, the limiting values calculated from the modulus format will be *different* in comparison to the calculated limiting values obtained from the normal presentation (24). If the dielectric spectrum is located in the given frequency window

$$\omega_{\min}\leqslant\omega\leqslant\omega_{\max}, \tag{34}$$

then the initial values of $\varepsilon_\mathrm{s}^{(0)}$and $\varepsilon_\infty^{(0)}$ can be found from the expressions

$$\varepsilon_\mathrm{s}^{(0)}=\max\left(\mathrm{Re}\,\varepsilon(\mathrm{j}\omega_{\min}),\quad Re\left(\frac{1}{\varepsilon(\mathrm{j}\omega_{\min})}\right)^{-1}\right),$$
$$\varepsilon_\infty^{(0)}=\min\left(\mathrm{Re}\,\varepsilon(\mathrm{j}\omega_{\max}),\quad Re\left(\frac{1}{\varepsilon(\mathrm{j}\omega_{\max})}\right)^{-1}\right). \tag{35}$$

One can also stress here a useful property of the complex function $R(j\omega)$, which helps to find the corrected values of ε_s and ε_∞. It is easy to see from (24) that for the given range of frequencies (34) this function should have a monotonic behavior, i.e.

$$R(\mathrm{j}\omega)\to\infty,\quad \text{at}\quad \omega\to\infty,$$
$$R(\mathrm{j}\omega)\to 0,\quad \text{at}\quad \omega\to 0. \tag{36}$$

Since the limiting values of ε_s and ε_∞ *cannot* be calculated precisely in any finite frequency window, one can suggest an iteration procedure for their self-consistent calculation. For this purpose one can present expression (32) in two equivalent forms

$$1+R\left(\mathrm{j}\omega;\quad \varepsilon_\mathrm{s}^{(n)},\varepsilon_\infty^{(n)}\right)=\frac{\varepsilon_\mathrm{s}^{(n-1)}-\varepsilon_\infty^{(n-1)}}{\varepsilon\left(\mathrm{j}\omega;\quad \varepsilon_\mathrm{s}^{(n-1)},\varepsilon_\infty^{(n-1)}\right)-\varepsilon_\infty^{(n-1)}},$$
$$1+R^{-1}\left(\mathrm{j}\omega;\quad \varepsilon_\mathrm{s}^{(n)},\varepsilon_\infty^{(n)}\right)=\frac{\varepsilon_\mathrm{s}^{(n-1)}-\varepsilon_\infty^{(n-1)}}{\varepsilon_\mathrm{s}^{(n-1)}-\varepsilon\left(\mathrm{j}\omega;\quad \varepsilon_\mathrm{s}^{(n-1)},\varepsilon_\infty^{(n-1)}\right)} \tag{37}$$

and consider these expressions as the self-consistent iteration procedure (SCIP) for the calculation of the limiting values ε_s and ε_∞ satisfying conditions of (36) and with initial values taken from expressions (35). Numerical verifications show that this SCIP is quickly convergent and helps to calculate the limiting values ε_s and ε_∞ *without* concrete knowledge of the complex function $R(\mathrm{j}\omega)$. The essential advantage of the SCIP is that it helps to extract the function $R(\mathrm{j}\omega)$ with acceptable accuracy and to calculate the rest of the fitting parameters related to this function only.

6. Treatment of the available complex permittivity data

We want to demonstrate the details of the new approach choosing the set of DS data for apple tissue (chosen from the whole set of data as the first in alphabetic order). DS data for the other fresh fruits and vegetables were treated in the same manner. The treatment process can be divided into four parts. The first part will be related to the analysis of the LF branch (region of increasing permittivity at low frequencies) that is always present in the data analyzed (see, for example Figs. 2 and 3).

6.1. Recognition of the LFD process

If initial data are presented in the RP format, one can notice that the tendency for increasing permittivity of the left-hand side branch disappears. See Fig. 4, where two files representing the temperature limits for available data (5 and 95 °C) are presented. If we suppose that in the LF region we have asymptotic behavior similar to expression (28), one can notice that the fitting procedure applied gives the exponent $\theta>1$ leading to the *negative* value of hopping conductivity $(\cos(\pi\theta/2))<0$ that contradicts the physical meaning of this value. So, one can conclude that we have at least some constant conductivity phenomenon ($\theta=1$) or, probably, a hidden conductance part expressed in the form of the Cole–Cole expression (when $|(\mathrm{j}\omega\tau)^\nu|)\gg 1$, which, however, is *not* detectable in the admissible frequency range. This means that after presentation of data in RP format a possible complex permittivity function can be presented in the form

$$\varepsilon(\mathrm{j}\omega)=\varepsilon_\infty+\frac{\sigma_0}{\mathrm{j}\omega}+\frac{\varepsilon_\mathrm{s}-\varepsilon_\infty}{1+R(\mathrm{j}\omega)}, \tag{38}$$

where the complex function $R(\mathrm{j}\omega)$ in (38) remains *unknown*. So, based on the initial hypothesis (38), one can subtract initially the conductance part $(\sigma_0/j\omega)$ and then apply the SCIP for calculation of

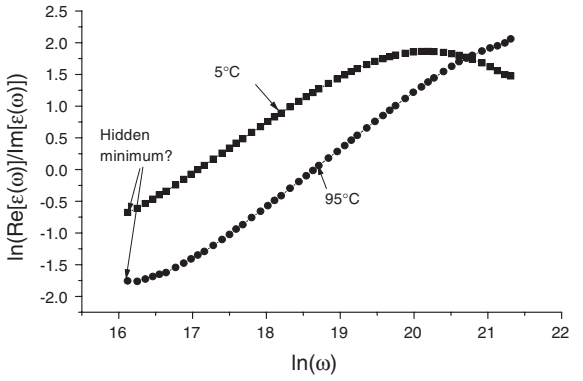

Fig. 4. The complex permittivity "apple.data" taken for the limiting temperatures 5 and 95 °C and presented in the ratio presentation (RP) format. From these plots it is possible to say that we have some conductance part and, probably, a hidden minimum, however, *unnoticeable* in the available frequency range.

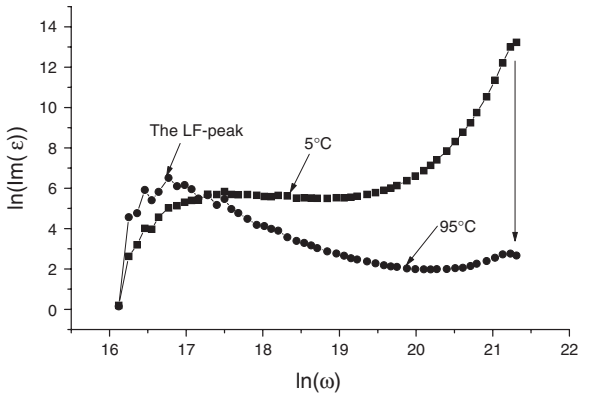

Fig. 5. The imaginary part of the complex permittivity after subtraction of the part (σ_0/ω) proportional to the constant conductivity. The corresponding values of σ_0 are: ($\sigma_0 = 1.9470 \times 10^9$ (5 °C), $\sigma_0 = 5.6581 \times 10^9$ (95 °C)). One can notice at least three branches (two extreme points at 5 °C. When the object is heated, the influence of the LF peak becomes more pronounced; however, the height of the HF peak decreases.

the limiting values ε_s and ε_∞. After subtraction of the conductance part (the fitting value σ_0 is calculated from the condition that $0 < \mathrm{Im}[\varepsilon(\omega_{\min})] < 0.2$), the imaginary part of the complex permittivity reveals other processes taking place in the HF range. Fig. 5 demonstrates the results of the subtraction procedure taken again for the limiting temperatures 5 and 95 °C, respectively.

6.2. Application of the self-consistent iteration procedure (SCIP)

Calculating the initial values of $\varepsilon_s^{(0)}$ and $\varepsilon_\infty^{(0)}$ from expressions (35), one can calculate the function $R(\mathrm{j}\omega)$ and verify the convergence of the whole procedure. These steps are illustrated by Figs. 6 and 7. As shown in Fig. 6, the complex function $R(\mathrm{j}\omega)$ has a tendency to satisfy the requirements of (36). The results of the application of the SCIP (Fig. 7) shows the quality of the fitting of the functions $\mathrm{Re}[\varepsilon(\omega)]$ and $\mathrm{Im}[\varepsilon(\omega)]$ (after subtraction) obtained with the help of calculated parameters ε_s and ε_∞.

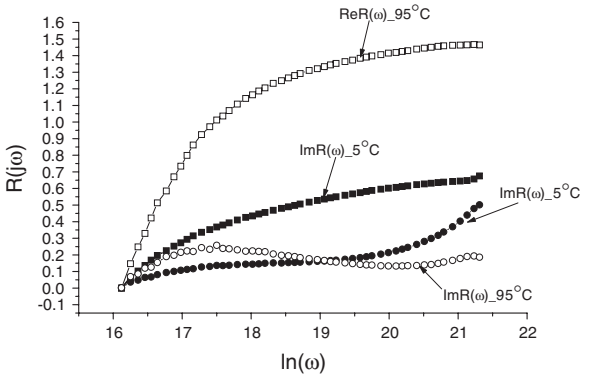

Fig. 6. The calculated complex function $R(\mathrm{j}\omega)$ after application of the SCIP. The final limiting values for ε_s and ε_∞ are: $\varepsilon_s = 100.6435$ (5 °C), $\varepsilon_\infty = 18.4406$ (5 °C), $\varepsilon_s = 99.7143$ (95 °C), $\varepsilon_\infty = 10.3424$ (95 °C).

6.3. Application of the separation procedure

For recognition of the number of power-law exponents, we are applying the separation procedure. Before its application, it is necessary to calculate the complex function $R(\mathrm{j}\omega)$ from expression (32)

$$R(\mathrm{j}\omega) = \frac{\varepsilon_s - \varepsilon(\mathrm{j}\omega)}{\varepsilon(\mathrm{j}\omega) - \varepsilon_\infty}, \tag{39a}$$

or from the expression representing the inverse function

$$R^{-1}(\mathrm{j}\omega) = \frac{\varepsilon(\mathrm{j}\omega) - \varepsilon_\infty}{\varepsilon_s - \varepsilon(\mathrm{j}\omega)}. \tag{39b}$$

This procedure involves the multiplication of the right-hand sides of equations (39) by the factor ω^s, where s (defined as the separation exponent) has a value between the power-law exponents v_1 and v_2 ($\min(|v_1|, |v_2|) < s < \max(|v_1|, |v_2|)$) with the opposite sign. This simple procedure helps to differentiate between the functions $R(\mathrm{j}\omega)$ defined by expression (24). This procedure applied to the

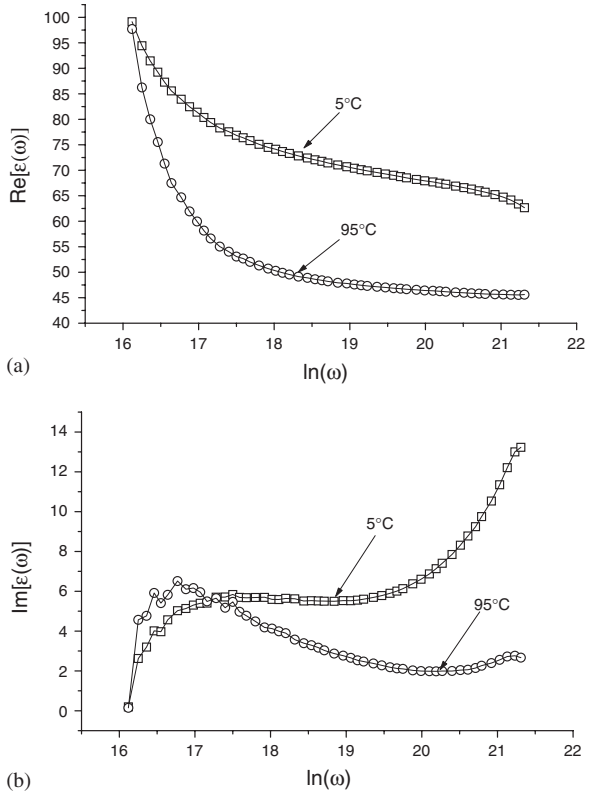

Fig. 7. (a) The application of the SCIP for the real values of the complex permittivity. The quality of the fitting is very good, which can be considered as the convergence of this iteration process. (b) The comparative plot for the imaginary part of the complex permittivity realized in the framework of the SCIP. The final values ε_s and ε_∞ are shown in the caption for Fig. 6.

function $R(j\omega) = (j\omega\tau_1)^{\nu_1} + (j\omega\tau_2)^{\nu_2}$ with negative separation factor ($s<0$) should give a ∪-shaped curve (the amplitudes $\tau_1^{\nu_1}, \tau_2^{\nu_2}$ have the same sign). The same procedure applied to the function $R(j\omega) = [(j\omega\tau_1)^{-\nu_1} + (j\omega\tau_2)^{-\nu_2}]^{-1}$ instead of the desired minimum leads to a 'hump' (∩-shaped curve). The separation procedure with positive factor ($s>0$) applied to the function $R^{-1}(j\omega) = (j\omega\tau_1)^{-\nu_1} + (j\omega\tau_2)^{-\nu_2}$ leads to the ∪-shaped curve and gives the 'hump' for the function $R^{-1}(j\omega) = [(j\omega\tau_1)^{\nu_1} + (j\omega\tau_2)^{\nu_2}]^{-1}$. This simple procedure helps to differentiate between collective motions connected in parallel from motions connected in series. For the concrete DS data, the application of this procedure leads to the conclusion that for *all* sets of the available data analyzed we have only *two* collective motions connected in series. In other words, the recognized fitting function has the form

$$R(j\omega) = [(j\omega\tau_1)^{-\nu_1} + (j\omega\tau_2)^{-\nu_2}]^{-1}. \tag{40}$$

We do not give the corresponding figures to save more space for the final results.

6.4. The application of the eigen-coordinates method

For more accurate calculation of the fitting parameters in expression (40) one can use the presentation which has been developed by one of the authors (RRN). This presentation was defined as the eigen-coordinates (ECs) method [25–28], in which the combination containing initially nonlinear fitting parameters is transformed into a set of straight lines. This transformation follows from the corresponding differential equation, in which the desired fitting parameters form a linear combination. Here we want to stress two important advantages related to the application of the ECs method:

(a) The ECs method does not require the initial estimate of the fitting parameters and thereby solves the problem of the *global* minimum.
(b) The ECs method uses the well-developed linear least-squares method (LLSM), which is rather stable with respect to the influence of the initial measured/experimental errors.

It is instructive to write the basic linear relationship (defined as the corresponding ECs) for the function

$$y(x) = A_1 \exp(\lambda_1 x) + A_2 \exp(\lambda_2 x). \tag{41}$$

This function is completely equivalent to the function $1/R(j\omega)$ obtained from expression (40). The corresponding linear relationship can be written in the following form:

$$Y(x) = C_1 X_1(x) + C_2 X_2(x) + C_3 X_3(x), \tag{42}$$

where

$$Y(x) = y(x) - \langle\cdots\rangle, \tag{43a}$$

$$X_1(x) = \int_{x_0}^{x} y(u)\,du - \langle\cdots\rangle, \quad C_1 = -(\lambda_1 + \lambda_2), \tag{43b}$$

$$X_2(x) = \int_{x_0}^{x} (x-u)y(u)\,du - \langle\cdots\rangle, \quad C_2 = -\lambda_1\lambda_2, \tag{43c}$$

$$X_3(x) = x - \langle\cdots\rangle. \tag{43d}$$

The symbol $\langle \cdots \rangle$ means that the corresponding arithmetic mean calculated for the function $X_k(x)$ ($k = 1,2,3$) should be subtracted from each $X_k(x)$ in obtaining the final expression. The constant C_3 in (42) contains the unknown value of the first derivative at the initial point and is not essential for calculation of the desired roots $\{\lambda_1$ and $\lambda_2\}$. The unknown constants A_1 and A_2 are also found using the LLSM from (41). The results of the fitting function $1/R(j\omega)$ are shown in Figs. 8a and b for the real and imaginary parts, respectively.

So, these four steps are sufficient for realization of the whole fitting procedure in order to obtain the complete set of fitting parameters (τ_1, ν_1, τ_2, ν_2, ε_s, ε_∞, and σ_0). These plots are shown in Figs. 9–15, respectively. Plots are shown for each of the nine fruits and vegetables in order to compare them with each other based on the corresponding fitting parameter.

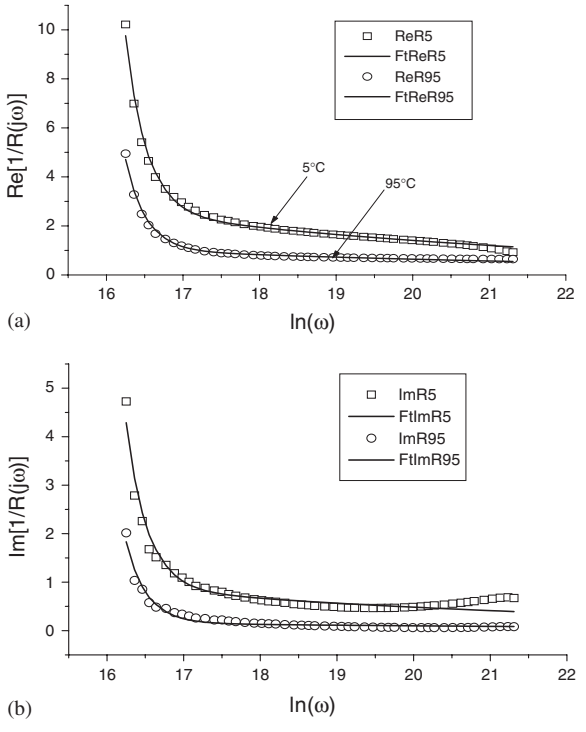

Fig. 8. (a) The calculated values of the function $\mathrm{Re}[1/R(j\omega)]$ (points) and their fitting functions found with the help of the ECs method. (b) The calculated values of the function $\mathrm{Im}[1/R(j\omega)]$ (points) and their fitting functions found with the help of the ECs method. One can notice that the fitting of the imaginary part is not as good as for the real part. In our opinion, it is related to the fact that the beginning of the third process in the HF-region is ignored.

7. Results and discussions

Finishing this analysis, in conclusion one can make the following statements:

1. Thanks to reduction of different micromotions to the averaged collective motion in the mesoscale region, which in the frequency domain is

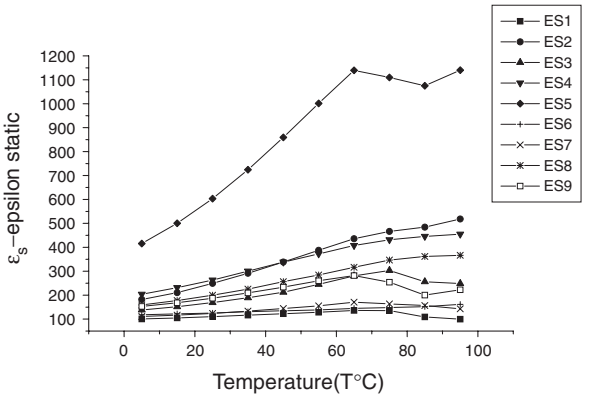

Fig. 9. The temperature dependence of the epsilon static parameter $\varepsilon_s(T)$ for all sets of the measured fruits and vegetables taken in alphabetical order: apple (1), avocado (2), banana (3), cantaloupe (4), carrot (5), cucumber (6), grape (7), orange (8), potato (9). Presumably, the behavior of this parameter is monotonic; after 65 °C some curves exhibit a break probably related to the destruction of cell membranes by high temperatures. Here and below the maximum value of the relative error in the finding of the fitting parameters do not exceed 5–6% and so the error interval is not shown.

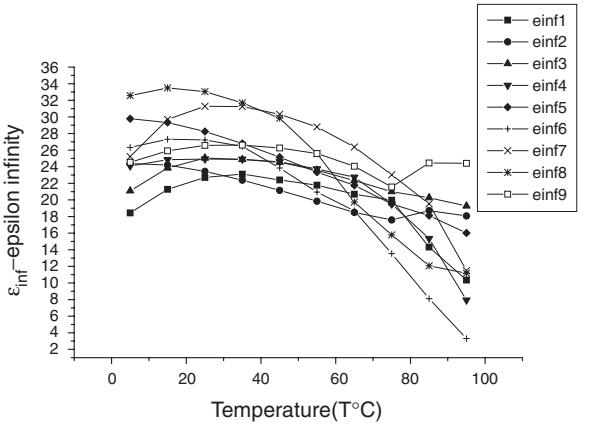

Fig. 10. The temperature dependence of the parameter $\varepsilon_\infty(T)$ for all sets of available fruits and vegetables taken, as in Fig. 9, in alphabetical order. This parameter can characterize the influence of the third HF-process. If this parameter is rather high, then the influence of the HF-process is becoming important; in the opposite case, when $\varepsilon_\infty(T)$ is low, the influence of the third process is not important.

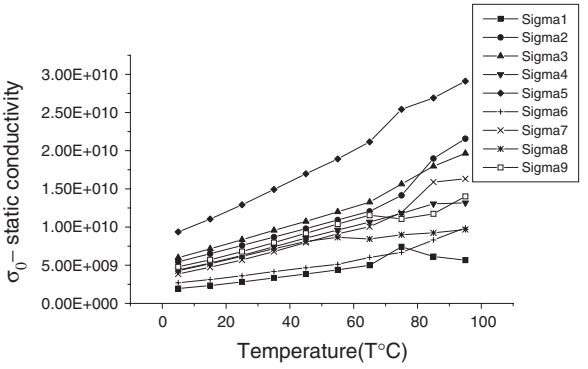

Fig. 11. The temperature dependence of the static conductivity parameter versus temperature. These plots reveal the common tendency, viz., the increasing of $\sigma_0(T)$ with increasing temperature.

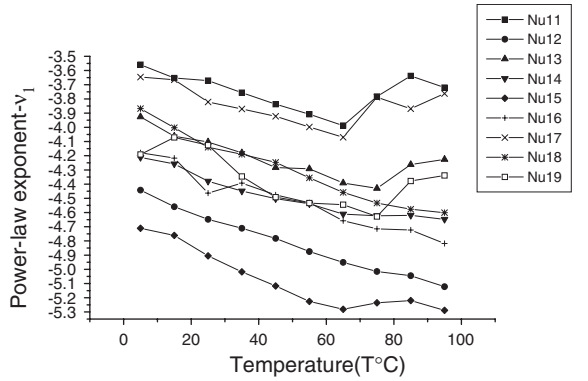

Fig. 12. Temperature dependence of the power-law exponent $v_1(T)$ for all sets of the plant tissues taken in alphabetical order.

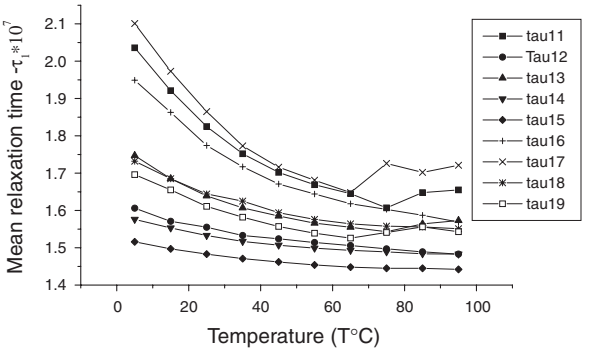

Fig. 13. Temperature dependence of the mean relaxation time τ_1. The ECs method provides the fitting values without initial estimates, and finally we obtained rather long relaxation times corresponding to the *global* minimum. These long relaxation times obtained are needed in further interpretations. The longest times belong to grape (7) tissue, and the shortest times represent carrot (5) tissue. One can notice that these data are correlated with those of Fig. 12.

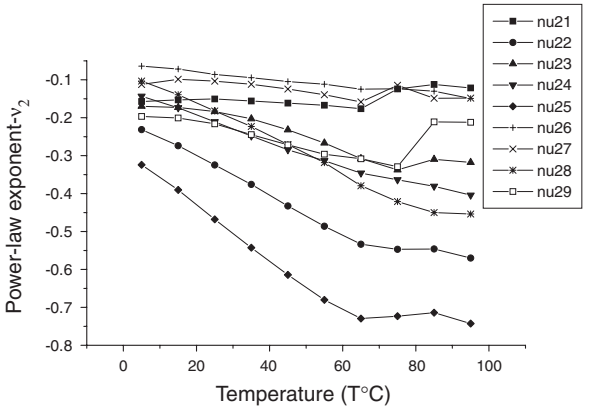

Fig. 14. The family of the power-law exponents related to $v_2(T)$. The values of all sets do not exceed unity. The quasi-monotonic behavior is disturbed again at temperatures exceeding 65 °C.

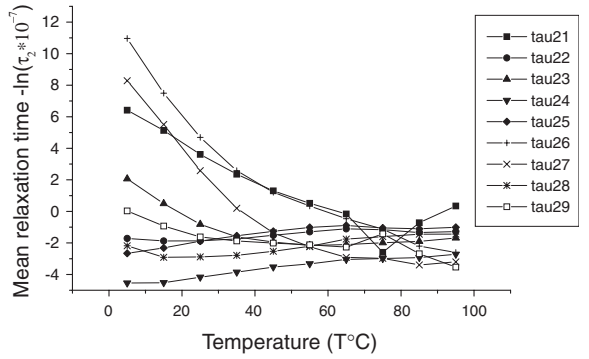

Fig. 15. The last family of plots demonstrates the behavior of the mean relaxation time $\tau_2(T)$. Because of strong deviations of these fitting parameters, this parameter is given in the normalized logarithmic form as $L_2 = \ln(\tau_2(T) \times 10^{-7})$.

expressed by the generalized memory function (23), it becomes possible to analyze different complex systems with the help of the complex permittivity function. It considerably increases the possibilities for potential usage of dielectric spectroscopy in analysis of systems having various complexities.

2. Applying this new ideology (reduction of a set of micromotions to averaged collective motion) to our concrete set of plant tissues one can notice that the identified fitting function remains *common* (38) for all measured samples of nine fresh fruits and vegetables. From this analysis, one can conclude that polar water contained in plant cells is retained as the main factor, completely 'specifying' their "electric" behavior.

3. After elimination of a large contribution of the conductive part caused by ion motion, one can notice at least two other processes (Fig. 5) that were completely hidden under the ionic conductance part. Measurements in the HF-region (especially at low temperatures) are implied to investigate these hidden processes in detail. One can notice that at higher temperatures the extreme HF process is disappearing.
4. Analyzing the final Figs. 9, 11, 12–15, one can notice that behavior for some fruits and vegetables becomes non-monotonic for temperatures exceeding 65 °C. Probably, this fact can be associated with the destruction of cell membranes by high temperatures. If this destruction takes place, the conductivity has a tendency to be increased, and other fitting parameters are decreased. This finding can be important for practical applications. The detection of instability of cell membranes with respect to temperature by the methods of dielectric spectroscopy can serve as a stimulus to investigate membrane instability due to other factors, including deterioration in quality or the influence of agricultural pests, etc.
5. Examination of fitting parameter values (Figs. 9–15) with respect to the non-electrical fruit and vegetable tissue characteristics listed in Table 2 did not reveal any apparent strong correlations. However, the power-law exponent v_1 (Fig. 12) showed some correlation with total soluble solids, indicative of sweetness, in that the three samples with highest sugar content (banana, grape, and apple) generally had higher values of v_1 than all the other tissues, and those with the lower sugar content (cucumber, avocado and carrot) had lower values of v_1.
6. This analysis can serve as an additional stimulus for investigation of qualitative factors which cannot be expressed quantitatively. Indeed, the complete fitting of the measured complex permittivity including its real and imaginary parts gives a unique possibility for finding an optimal set of these fitting parameters for constructing so-called calibration curves when some qualitative factor can be expressed in terms of these parameters. The simplification achieved in the process of the identified collective motions that can then be identified with the help of specially developed fitting procedures makes this problem achievable for numerous practical applications.

References

[1] S.O. Nelson, IEEE Trans. Electr. Insul. 26 (1991) 845.
[2] S.O. Nelson, J. Microwave Power 12 (1977) 67.
[3] S.O. Nelson, Trans. ASAE 23 (1980) 1314.
[4] S.O. Nelson, Trans. ASAE 26 (1983) 613.
[5] S.O. Nelson, W.R. Forbus Jr., K.C. Lawrence, J. Microwave Power Electromagn. Energy 29 (1994) 81.
[6] S.O. Nelson, W.R. Forbus Jr., K.C. Lawrence, Trans. ASAE 38 (1995) 579.
[7] S.O. Nelson, Trans. ASAE 46 (2003) 567.
[8] C.J.F. Bőttcher, P. Bordewijk, Theory of Electric Polarization, Elsevier, Amsterdam, 1992.
[9] Yu. Feldman, A. Puzenko, Ya. Ryabov, Chem. Phys. 284 (2002) 139.
[10] A.K. Jonscher, Dielectric Relaxation in Solids, Chelsea Dielectric Press, London, 1983.
[11] H. Mori, Progr. Theor. Phys. 30 (1963) 578;
R. Zwanzig, in: W.E. Brittin, B.W. Downs, J. Downs (Eds.), Lectures in Theoretical Physics, vol. III, Interscience Publ. Inc., New York, 1961, pp. 106–141.
[12] R.M. Yulmetuev, N.R. Khusnutdinov, J. Phys. A 27 (1994) 5363.
[13] V.Yu. Shurygin, R.M. Yulmetuev, Zh. Eksp. Teor. Fiz. 96 (1989) 938 (Sov. JETP 69 (1989) 532 and references therein).
[14] Y.P. Kalmykov, S.V. Limonova, J. Mol. Liq. 43 (1989) 71.
[15] R.M. Yulmetuev, Phys. Lett. 56A (1976) 387.
[16] V.I. Arkhipov, A.Yu. Zavidonov, J. Mol. Liq. 106/2–3 (2003) 155.
[17] V.I. Arkhipov, J. Non-Cryst. Solids 305 (2002) 127.
[18] R.R. Nigmatullin, S.I. Osokin, G. Smith, J. Phys. D 36 (2003) 2281.
[19] R.R. Nigmatullin, S.I. Osokin, G. Smith, J. Phys. C: Condens. Matter 15 (2003) 3481.
[20] R.R. Nigmatullin, S.I. Osokin, J. Signal Proc. 83 (2003) 2433.
[21] V.I. Arkhipov, private communication.
[22] R.R. Nigmatullin, Ya.E. Ryabov, Phys. Solid State 39 (1997) 87;
R.R. Nigmatullin, Ya.E. Ryabov, Russ. Phys. J. 40 (1997) 314.
[23] A. Le Mehaute, R.R. Nigmatullin, L. Nivanen, Fleches du Temps et Geometrie Fractale, Hermez, Paris, 1998.
[24] R.R. Nigmatullin, A.L. Mehaute, Georesources 1(8) (2004) 2. (Extended version of this paper has been recently published in J. Non-Cryst. Solids 351 (2005) 2888.)
[25] R.R. Nigmatullin, M.M. Abdul-Gader Jafar, N. Shinyashiki, S. Sudo, S. Yagihara, J. Non-Cryst. Solids 305 (2002) 96.
[26] M.M. Abdul-Gader Jafar, R.R. Nigmatullin, Thin Solid Films 396 (2001) 280.
[27] R.R. Nigmatullin, Physica A 285 (2000) 547.
[28] R.R. Nigmatullin, G. Smith, Physica A 320 (2003) 291.